nature chemistry

Article

https://doi.org/10.1038/s41557-025-01762-7

Aging-dependent evolving electrochemical potentials of biomolecular condensates regulate their physicochemical activities

Received: 8 January 2024

Accepted: 29 January 2025

Published online: 12 March 2025

Check for updates

Wen Yu[1,5], Xiao Guo[1,5], Yu Xia[2,5], Yuefeng Ma[1,5], Zhongli Tong[1], Leshan Yang[1], Xiaowei Song[2], Richard N. Zare[2] ✉, Guosong Hong[3] ✉ & Yifan Dai[1,4] ✉

A passive consequence of macromolecular condensation is the establishment of an ion concentration gradient between the dilute and dense phases, which in turn governs distinct electrochemical properties of condensates. However, the mechanisms that regulate the electrochemical equilibrium of condensates and their impacts on emergent physicochemical functions remain unknown. Here we demonstrate that the electrochemical environments and the physical and chemical activities of biomolecular condensates, dependent on the electrochemical potential of condensates, are regulated by aging-associated intermolecular interactions and interfacial effects. Our findings reveal that enhanced dense-phase interactions during condensate maturation continuously modulate the ion distribution between the two phases. Moreover, modulating the interfacial regions of condensates can affect the apparent pH within the condensates. To directly probe the interphase and interfacial electric potentials of condensates, we have designed and implemented electrochemical potentiometry and second harmonic generation-based approaches. Our results suggest that the non-equilibrium nature of biomolecular condensates might play a crucial role in modulating the electrochemical activities of living systems.

Biomolecular condensation is emerging as a generic mechanism for organizing cellular processes through the selective partitioning of certain biomolecules into a membraneless organelle[1–4]. Phase separation, a typical mechanism of biomolecular condensation, results in a density transition in the solution system[5,6]. Accordingly, the impacts of a macromolecular phase transition extend beyond the specific sets of biomolecules involved in the formation of biomolecular condensates, and also encompass the ion and water environments[7–10]. Studies have revealed that the dense-phase chemical environment of condensates is distinct from the coexisting dilute phase[10–15], as exemplified by pH and ion gradients across the two phases[10,14,16,17]. An emergent function of condensation is modulating cellular chemical environments by regulating the distribution of water molecules and ions[9,18], emphasizing the critical importance of the electrochemical features of condensates for defining their functions. These electrochemical properties of the condensate microenvironment also suggest that condensates are chemically active and can dictate chemical functions through their unique electrochemical environments[10,14,19–22], such as promoting redox reactions via the ion

[1]Department of Biomedical Engineering, Washington University in St Louis, St Louis, MO, USA. [2]Department of Chemistry, Stanford University, Stanford, CA, USA. [3]Department of Materials Science and Engineering, Stanford University, Stanford, CA, USA. [4]Center for Biomolecular Condensates, Washington University in St Louis, St Louis, MO, USA. [5]These authors contributed equally: Wen Yu, Xiao Guo, Yu Xia, Yuefeng Ma. ✉e-mail: zare@stanford.edu; guosongh@stanford.edu; dyifan@wustl.edu

https://doi.org/10.1038/s41557-025-01762-7

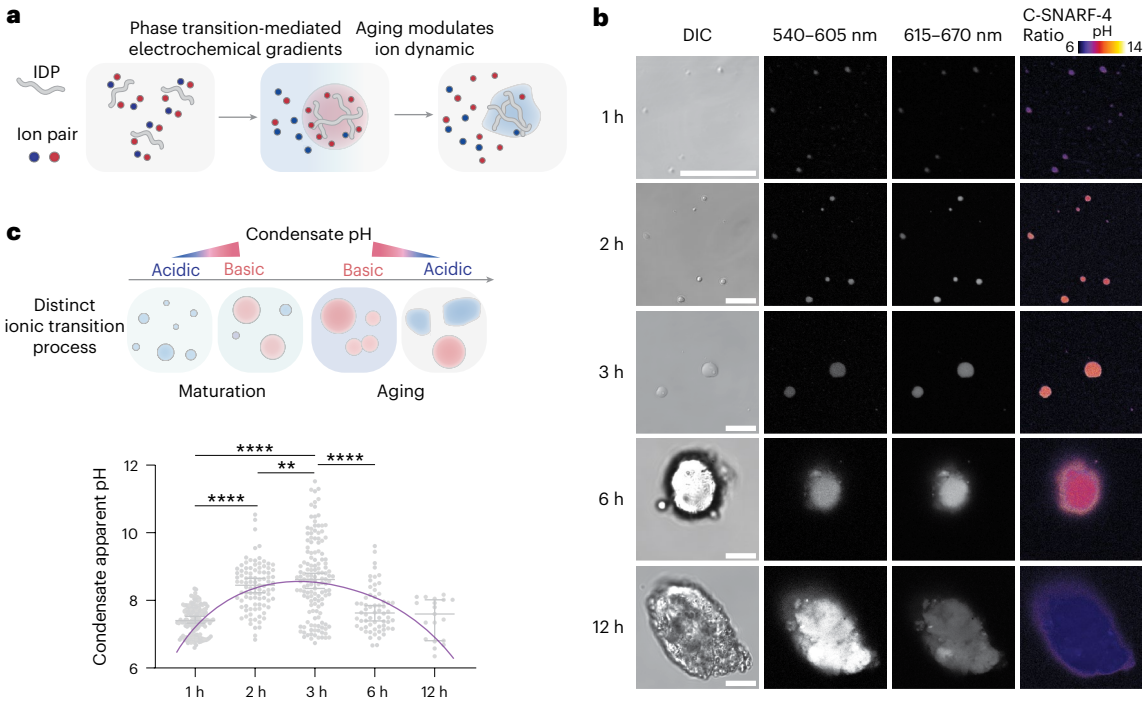

Fig. 1 | The aging-dependent internal pH transition of biomolecular condensates. a, The phase transition of an IDP mediates a switch of interactions from IDP–solvent to IDP–IDP, which results in an asymmetric distribution of ions, leading to a unique condensate electrochemical environment. Aging of the condensates further modulates the dense-phase molecular interactions, which in turn should modulate the condensate ionic environment. **b**, Representative C-SNARF-4 ratiometric images of RLP condensates aged for different periods. C-SNARF-4 dye was added into the sample 30 min before imaging. Ratiometric images were acquired by dividing the image at 615–670 nm by the image at 540–605 nm. The rainbow colour bar (blue to red) indicates acidic to basic pH conditions. Scale bars, 10 µm. **c**, Quantitative analysis of condensate pH using global particle analysis, showing a two-stage transition of dense-phase pH from acidic to basic to acidic throughout the maturation and aging process, after condensate formation. Each data point represents an individual condensate. Statistical analysis was performed using a two-tailed *t*-test: $^{****}P < 0.0001$, $^{**}P = 0.0073$. Data points represent mean ± s.d. $n > 18$ condensates.

gradient-dependent interfacial electric field of the condensates[10,23,24]. Despite the critical roles of electrochemical environments in diverse cellular functions[25], such as regulating translation, stress responses and intercellular communication[26–28], as well as the ubiquitous existence of condensates intracellularly[29], our understanding of the mechanisms with which biomolecular condensates regulate the electrochemical dynamics of their microenvironment is currently lacking.

In this Article, we explore the electrochemical dynamics of condensates throughout their maturation and aging processes. The maturation and aging of condensates are crucial processes underlying the dysregulation of physiological condensates and the function of pathological condensates[30,31]. The formation of condensates is largely described in the framework of liquid–liquid phase equilibria[29,32]. However, condensates exist in a non-equilibrium state[33–36]. For example, condensates exhibit time-dependent changes in material properties such as viscoelasticity and rheology[37,38]. These features arise from constantly changing protein–protein and protein–solvent interactions[34,39]. We thus wondered whether such driving forces would also affect the mesoscopic electrochemical environments of condensates and how the microenvironments in turn might modulate the chemical and physical activities of condensates.

In this study, we have discovered that the maturation and aging processes of condensates influence their electrochemical equilibrium. This occurs via a liquid-to-gel transition and an interfacial effect affecting the electric double layer. These characteristics directly manifest in the age-dependent electric potential differences between the phases, which was evaluated with electrochemical potentiometry and by assessing the interfacial electric potential using a second harmonic generation (SHG) technique. These findings reveal a detailed mechanism whereby the dynamic nature of the condensates is reflected in the evolving electrochemical potentials of the condensates. Furthermore, we have established a correlation between the electrochemical features of condensates and their chemical and physical activities. We explore this correlation in three distinct cases: (1) electrochemical redox reactions, (2) the transportation of a charged small molecule and (3) spatial modulation of amyloid fibril formation. Our study has revealed a previously unknown operational mechanism of condensates, wherein their functions can be manipulated by their intrinsic electrochemical dynamics. This functional mechanism extends our understanding of condensate functions beyond the biomolecular functions encoded in specific sets of biomolecules.

Results

The formation of condensates can be mediated by multivalent biomacromolecules, such as intrinsically disordered proteins (IDPs)[40]. In this study, we utilized the wild-type resilin-like polypeptide (RLP) as our model system. RLP has the amino-acid sequence Ser-Lys-Gly-Pro-[Gly-Arg-Gly-Asp-Ser-Pro-Tyr-Ser]$_{20}$-Gly-Tyr, which exhibits high similarity in its sequence features to native IDPs such as the disordered regions of FUS and Ddx4 (refs. 41,42). This model system has been widely used in studying sequence-dependent phase behaviour and condensate features[43], and is known to mediate a pH gradient between phases[10].

Condensate aging-dependent ionic environments

We first explored whether the ionic environments of condensates undergo changes during a maturation and aging period of 12 h (Fig. 1a). To this end, we employed an established ratiometric fluorescent method using the C-SNARF-4 dye[10,14,17], which was used at a low concentration (200 nM) to prevent interference with protein phase behaviours, to measure the dense-phase pH of the condensates.

We calibrated the signal of the C-SNARF-4 dye against an external pH meter and verified the pH measurements using artificially created crowded solution environments[44] (Supplementary Fig. 1). We then used this method to capture ratiometric and differential interference contrast (DIC) images to assess the global changes in condensate pH.

During the first 2 h after phase separation, we observed a time-dependent shift in condensate pH from neutral to basic. From the third hour to the twelfth hour, the internal pH of the condensates showed a transition from basic to acidic pH (Fig. 1b). These changes were independent of the existence of crowding agents, as we observed the same trend in aging-dependent condensate pH with condensates formed via different strategies without added crowding agents (Supplementary Fig. 2). These observations confirm that the ionic environment of the condensates undergoes changes in relation to aging. The two-stage transition in the condensate pH, from neutral to basic and then back to acidic (Fig. 1c), suggests that the temporal dynamics of condensate ionic environments are governed by distinct physicochemical features.

The liquid-to-gel transition modulates condensate pH

We next delved into the underlying mechanism responsible for the modulation of condensate ionic environments. We initially hypothesized that condensate aging, particularly the liquid-to-gel transition[45] resulting from increased inter/intrachain interactions in the dense phase, influences the internal ionic content (Fig. 1a). This change could be instigated by a shift in the interactions from protein–solvent to protein–protein during the aging process, consequently altering the ion contents of the condensates.

To validate whether there was an enhanced interaction in the dense phase during this aging period, we used a thioflavin T (ThT) assay to evaluate whether enhanced inter/intramolecular interactions take place in the dense phase of condensates. Even though condensates formed immediately after the ionic strength decreased (Supplementary Fig. 3a), the ThT signal only started to increase sharply at ~2 h of incubation. This suggests that the condensates are undergoing a change in inter/intramolecular interactions from the 2-h timepoint. We next employed a molecular rotor-based boron dipyrromethene fluorophore (BODIPY)-based assay, an established strategy to characterize the microviscosity of condensates based on the change in fluorescence lifetime of the BODIPY[13]. The viscosity of the dense phase has been used to reflect the strength of intra/intermolecular interactions in the dense phase[13]. Compared to a condensate sample incubated for 2 h, we observed an increase in the fluorescence lifetime of BODIPY in the condensate sample incubated for 6 h (Supplementary Fig. 3b), confirming that the intra/intermolecular interactions in condensates were enhanced during the aging process. Next, we investigated the translational diffusion dynamics of proteins in the condensates by means of fluorescence recovery after photobleaching (Supplementary Fig. 3c). A slower fluorescence recovery was observed in aged condensates compared to younger condensates. We also used fluorescein-labelled dextran molecules to evaluate whether the mesh size of the condensates changed during the aging process. A notable exclusion effect was observed for aged condensates compared to the condensates before aging (Supplementary Fig. 3d). These tests collectively confirm that, during the aging period we evaluated, there were changes in the dense-phase interactions and physical properties of the RLP condensates.

We next evaluated the pH of condensates of similar sizes but with different aging periods. A decrease in dense pH from ~8.5 to ~7.3 was observed during the aging process (Fig. 2a). Interestingly, for aged condensates, a core–shell-structured pH gradient was observed for condensates aged over 8 h, with a lower pH in the core and a higher pH at the shell of the condensates. This feature aligns with recent discoveries indicating that condensates possess distinct internal structures between their core and shell[46,47], possibly driven by the differences in IDP conformations between the core and shell[48]. In an extreme case, for condensates aged for 24 h, compared to spherical condensates, a gel-like, non-spherical assembly possesses a more acidic dense phase (Fig. 2b). Similarly, when we analysed condensates that had been aged the same but had distinct sizes, we found that condensates with smaller sizes showed a more acidic pH (Fig. 2c). These observations suggest that the interfacial regions might play a key role in modulating the condensate interior pH. However, this might also imply that condensates, as a consequence of their different sizes, might possess distinct maturation histories that can determine their ionic environments. These observations confirm that, during the aging process, the dynamics of dense-phase ionic environments correlate with enhanced dense-phase interactions and changes in condensate structure.

Interfaces regulate the interior ionic environment

The observation that condensates possess a large interfacial region in which an apparent ionic gradient is observed suggests that, due to the soft nature of the condensate interface[49,50], the interfacial region can contribute to determining the dense-phase ionic environment of the condensates. To specifically evaluate the contribution of these interfacial regions, we devised the following two assays to disrupt—actively or passively—the interfacial regions and assess whether a change in dense-phase pH could be triggered.

We first doped sodium dodecyl sulfate (SDS), an amphipathic anionic surfactant consisting of a hydrophobic hydrocarbon chain and a hydrophilic head group, onto the surfaces of the condensates[49], to perturb the interfacial structure or surface charge of the condensates by altering their surface chemical constituents[49] (Fig. 2d). We confirmed that the addition of 0.1 mM SDS did not alter the phase behaviour of the RLP condensates, as evaluated by a partitioning assay of RLP-superfolder green fluorescent protein (Supplementary Fig. 4a). We then evaluated and compared the pH of condensates with similar sizes in samples with and without SDS. The addition of SDS significantly changed the dense-phase pH of the condensates (Fig. 2d), suggesting the importance of the interfacial properties in determining the dense-phase pH.

To determine whether there might be a charge-dependent effect caused by the surfactant, given that SDS is an anionic surfactant, we next used cetyltrimethylammonium bromide (CTAB), a cationic surfactant, to evaluate the dense-phase pH. As before, we did not observe a significant change in the phase behaviour of the RLP condensates (Supplementary Fig. 4a). When compared to the effects mediated by the addition of SDS, despite CTAB having a longer hydrogen chain, which should affect the interfacial structure to a greater extent, the addition of 0.1 mM CTAB did not significantly alter the dense-phase pH (Fig. 2d). These observations suggest that the surface charge properties of condensates might contribute to the regulation of the ionic environments of the condensates.

Second, inspired by the role of the surface charges of a solid in modulating the interfacial activity of contacted water droplets[51,52], we incubated the condensates on an uncoated surface or a surface modified with positively charged poly-d-lysine and assessed the internal pH of condensates in contact with the respective surfaces (Fig. 2e). We hypothesized that, with an electric double layer established by a positively charged surface, the overlapping of the electric double layers of the condensates and the surface should lead to either the desorption of surface ions or a change in interfacial potential to maintain the adsorption of ions on the surface[53]. Due to the correlation between surface electric charges and surface tension[54,55], these factors might also contribute to the changes in the surface structure of condensates driven by interfacial electrostatic interactions, thereby altering the dense-phase pH. Indeed, we found that condensates in contact with a positively charged surface exhibited a significantly higher internal pH compared to condensates in contact with an uncharged surface (Fig. 2e). Using *z*-stack imaging on the same sample incubated on a

https://doi.org/10.1038/s41557-025-01762-7

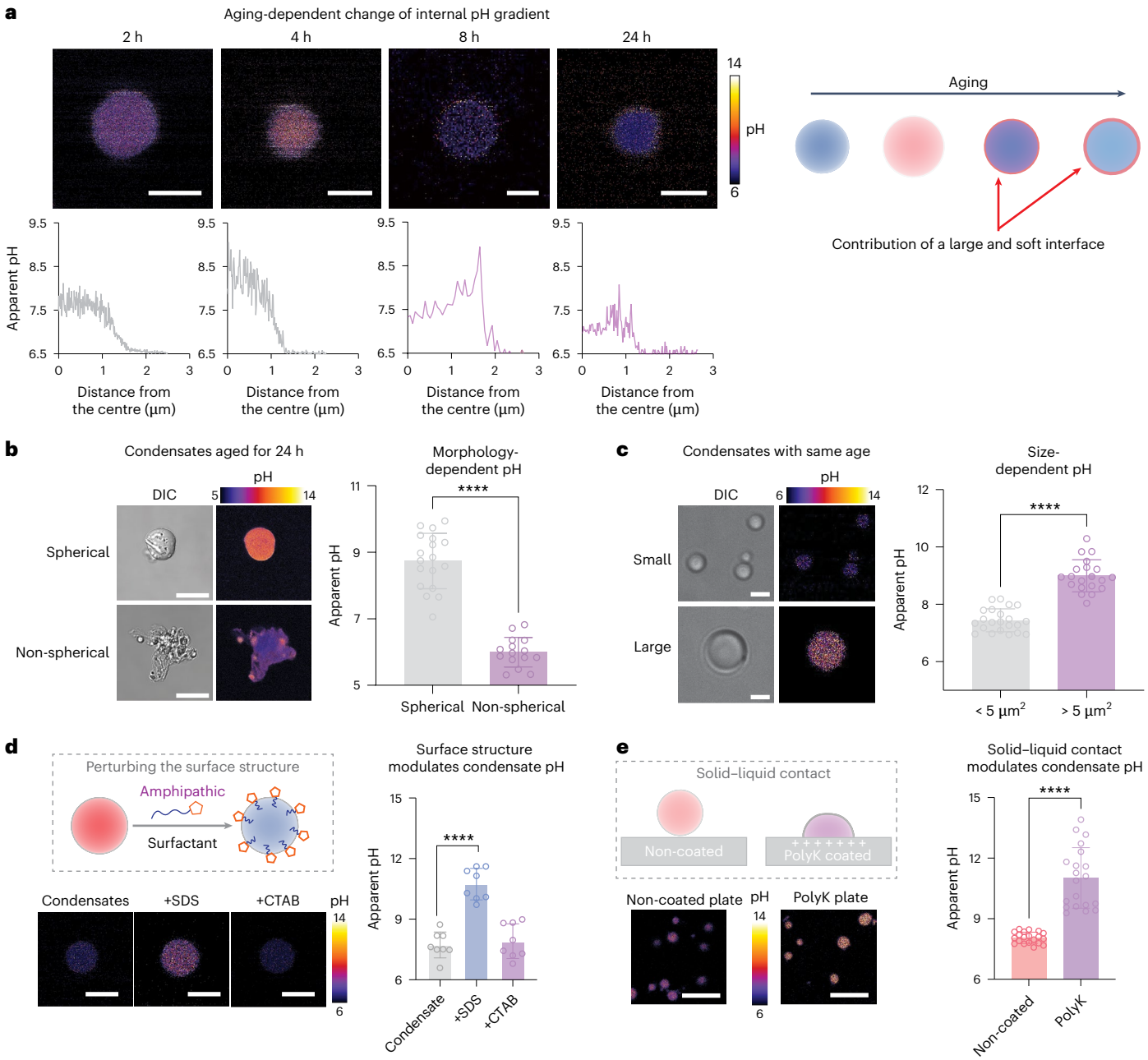

Fig. 2 | The aging-dependent interfacial structure of condensates affects condensate pH. a, Representative images of condensates with different ages and similar size show that aging alters the internal pH gradient of the condensates. Scale bars, 2 μm. **b**, Condensates aged for the same period, with distinct morphology, show distinct internal pHs. Statistical analysis was performed using a two-tailed *t*-test: ****$P < 0.0001$. Scale bars, 10 μm. Data points represent mean ± s.d. $n > 14$ condensates. **c**, Evaluation of the size-dependent internal pH of condensates aged for 3 h. Internal pH was compared for condensate cross-sectional areas below and above 5 μm². Statistical analysis was performed using a two-tailed *t*-test: ****$P < 0.0001$. Scale bars, 2 μm. Data points represent mean ± s.d. $n > 19$ condensates. **d**, Evaluation of the effect of modulating the interfacial structure of condensates on internal pH through a surfactant-based assay. The addition of anionic surfactant perturbed the internal pH. Statistical analysis was performed using a two-tailed *t*-test: ****$P < 0.0001$. Scale bars, 2 μm. Data points represent mean ± s.d. $n = 8$ condensates. **e**, Evaluation of the interface-dependent modulation of internal pH through a solid–liquid contact assay. Contact between the charged surfaces affects surface electrostatic conditions and interfacial structure, thereby modulating the internal pH. PolyK represents poly-lysine. Statistical analysis was performed using a two-tailed *t*-test: ****$P < 0.0001$. Scale bars, 10 μm. Data points represent mean ± s.d. $n = 20$ condensates.

positively charged surface, condensates with no contact with the solid surface (within the solution phase) showed a notably different internal pH comparing to condensates residing on the solid surface (Supplementary Fig. 4b). This observation confirms that the reorganization of surface charge or interfacial potential induced by solid–liquid contact can potentially serve as a factor affecting the dense-phase pH. Both observations support the role of the interface in modulating the ionic environments of condensates, and these interfacial effects can possibly be attributed to the distinct structure of the soft interfacial region and the electrostatic charge condition of the condensates surface.

pH gradient and interphase electric potential of condensates

As illustrated by Donnan equilibrium and theory based on the electrochemical potential equilibrium between phases[56,57] (details are provided

https://doi.org/10.1038/s41557-025-01762-7

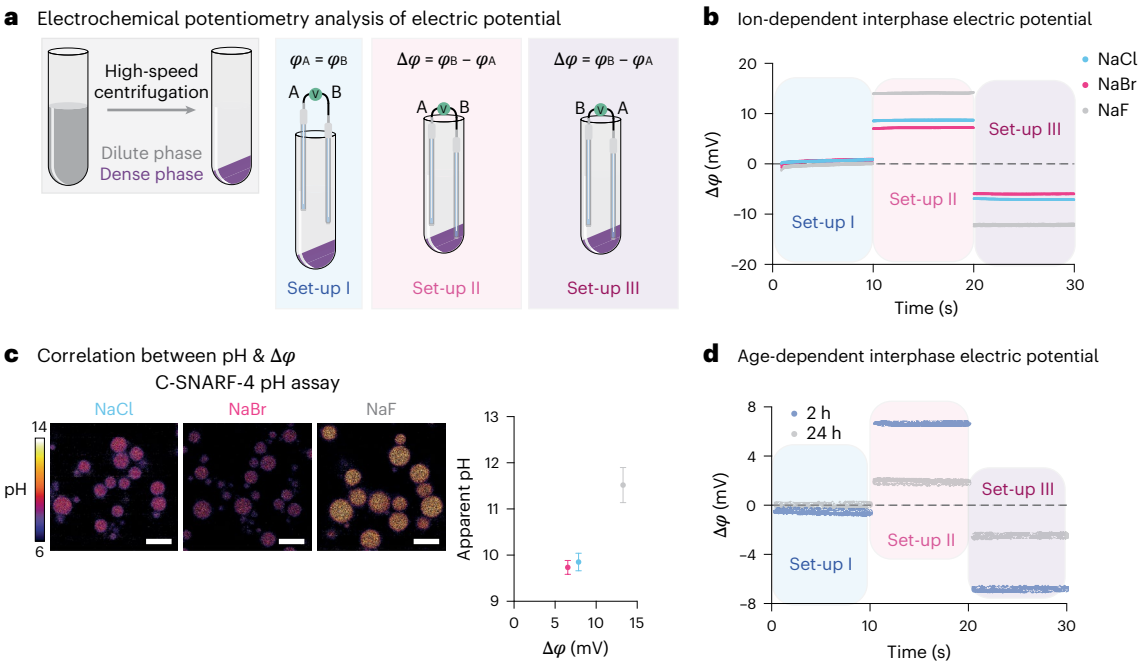

Fig. 3 | Analysing the interphase electric potential with electrochemical potentiometry. a, Bulk separation of phases was achieved by high-speed centrifugation, resulting in spatially distinct dilute and dense phases, followed by direct electrochemical potentiometry measurements of the electric potential difference between the dilute and dense phases. Set-up I shows two electrodes in the same phase. Set-up II shows two electrodes in distinct phases. Set-up III shows the switch of working and counter electrodes. **b**, Measurements of the electric potential difference between phases for a condensate sample prepared in different salt conditions and incubated for 2 h. Open-circuit potential measurements (10 s) were performed with the two-electrode set-up. RLP condensates were incubated for 2 h in 50 mM Tris pH 7.5 with distinct types of salt (150 mM NaCl, NaBr or NaF). The coloured bands correspond to distinct set-up showed in **a**. **c**, Correlation between interphase electric potential and the interior pH of the condensates. Data points represent mean ± s.d. $n = 3$ samples from three independent experiments. Scale bars, 5 µm. **d**, Measurements of the electric potential difference between phases for a condensate sample prepared in 150 mM NaCl and incubated for 2 h and 24 h. The coloured bands correspond to distinct set-up showed in **a**.

in Supplementary Text 1), the interphase pH gradient is directly correlated with the electric potential gradient between phases, which in turn should be determined by the types of ionic content in the solution[58]. To understand this, we set out to investigate the correlation between interphase electric potential and the internal pH of condensates by dialysing the condensate solution into different solutions containing 150 mM alkali halides, specifically NaCl, NaBr and NaF.

To enable the analysis of interphase electric potential directly, we first devised and implemented an electrochemical potentiometry set-up[57,59]. This set-up allowed direct measurements of the difference in electric potential between the dilute and dense phases, instead of indirectly deriving it by considering the individual activities of proteins, water and ions. To this end, we used high-speed centrifugation[43] to achieve spatial separation of the dilute and dense phases after condensate formation for different periods (Fig. 3a). This resulted in a system akin to an aqueous two-phase system[60], where two phases coexist in equilibrium with a well-defined physical boundary, allowing direct probing of the electric potential difference between phases using an external electrode-based system[61]. Two identical Ag/AgCl capillary electrodes, denoted electrode A and electrode B (in 3 M KCl solution), were simultaneously used to measure the electric potential (φ_A–φ_B) in the different phases (Fig. 3a)[62]. The measured potential difference between these two electrodes represents the potential drop difference between the liquid junctions of the dilute phase/Ag/AgCl and dense phase/Ag/AgCl.

Electrical potential measurements were performed on condensates prepared in different salts. To ensure measurement accuracy, we initially immersed the two electrodes in the same dilute phase and observed no difference in electric potential (Fig. 3b), indicating identical electrochemical behaviour of the two electrodes. Subsequently, we immersed one electrode into the dense phase while keeping the other in the dilute phase, showing a clear potential difference in the positive region (Fig. 3b). On switching the positions of the electrodes, we observed a similar level of potential difference in the negative range, confirming the robustness of the measurements. We found that condensates formed in NaF solution showed the biggest interphase potential difference compared to those formed in NaCl or NaBr solutions (Fig. 3b). This could be attributed to differences in the free energy of hydration among these salts[63,64], with F^- having the lowest free energy of solvation in water and thus being the strongest potential-determining ion. All measurements showed a positive electric potential in the dense phase, which aligns with our pH measurements, with a more basic internal pH compared to the dilute phase being observed for all condensates (Fig. 3c; Supplementary Text 1 provides an explanation of the theoretical relationship). The level of basicity in the dense phase corresponds to the differences in interphase electric potentials. These observations provide direct evidence of the existence of an interphase electric potential in condensate systems and illustrate the relationship between condensate pH and interphase electric potential.

Aging-dependent interphase electric potentials

The use of electrochemical potentiometry to directly analyse interphase potential gradients allowed us to study the aging-dependent interphase potential. As such an analysis is conducted by separating the solution into two distinct bulk phases, the information obtained from bulk-phase analysis primary reflects the internal condition of the dense phase and largely minimizes the contribution of the interfacial region due to the existence of a single interfacial region. Owing to the substantial amount of protein required for such measurements, we assessed the interphase electric potentials using a condensate solution aged

https://doi.org/10.1038/s41557-025-01762-7

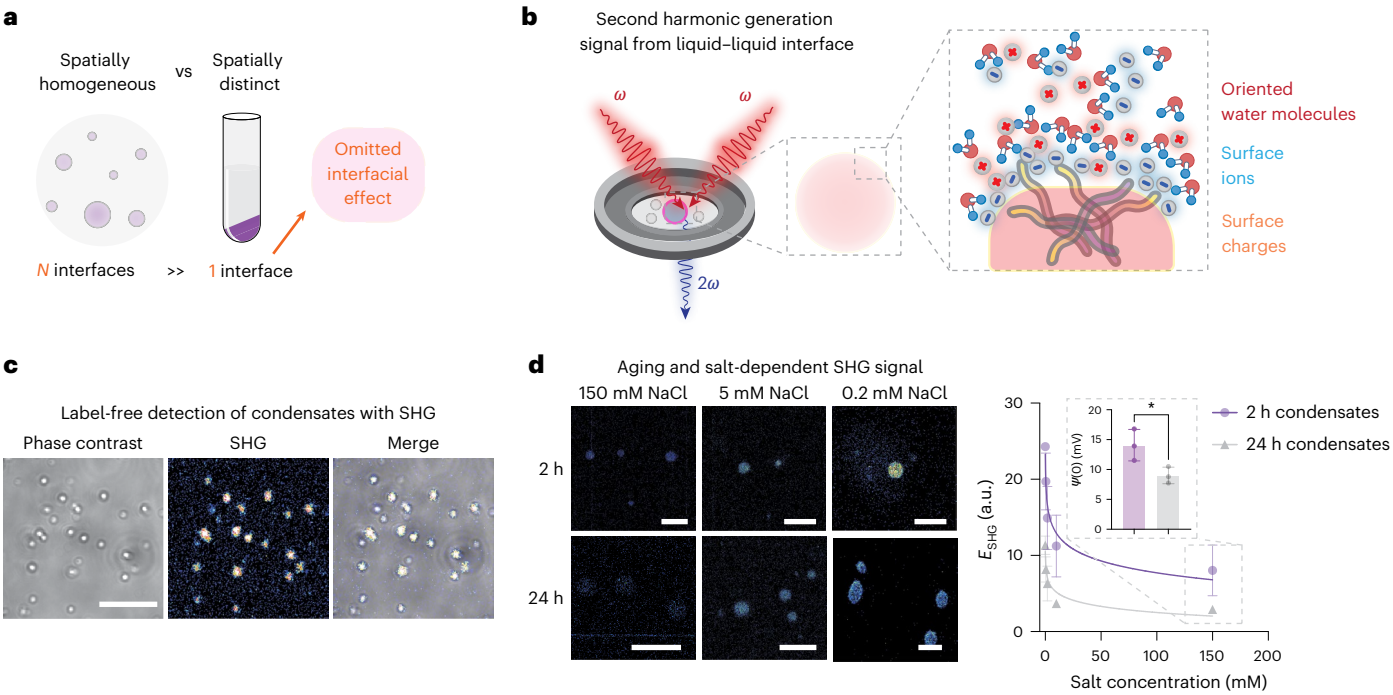

Fig. 4 | Evaluation of aging-dependent surface potentials of condensates with SHG. a, A key difference between spatially separated bulk phases and condensates in solution is the existence of different quantities of interfaces. **b**, Effect of SHG for the label-free evaluation of the liquid–liquid interface of condensates. The surface electric field modulates the alignment of water molecules, leading to non-centrosymmetry at the interface, which generates an SHG signal. **c**, Direct visualization of condensates using the SHG effect. Sixteen-colour coding was used to represent the SHG signal. Scale bar, 10 µm. **d**, Comparison of the interfacial SHG signal of condensates incubated for 2 h and 24 h under different salt conditions. The signal obtained from condensates of similar size was fitted with Gouy–Chapman theory to quantify the surface potential of the condensates. The inset graph shows a comparison of the surface potential of condensates under the 150 mM NaCl condition. Scale bars, 10 µm. Statistical analysis was performed using a two-tailed *t*-test: *$P = 0.0419$. Data points represent mean ± s.d. $n = 3$ independent experiments.

for 2 h and 24 h (Fig. 3d). Condensate samples aged for 2 h exhibited a potential difference of ~6.7 mV between phases, whereas those aged for 24 h showed a potential difference of ~2.2 mV. The decreased phase potential difference aligns with the reduced pH gradients between phases observed during condensate aging. This observation confirms that the evolving electric potentials strongly correlate with the ionic environments within the dense phase[65].

SHG analysis of the interfacial field of individual condensates

As shown in previous sections, the interfacial regions might serve a role in regulating dense-phase ionic content. However, the use of bulk-phase electrochemical measurements does not provide information about the individual interfaces of condensates (Fig. 4a). To understand the interfacial effect at a single condensate level, we used SHG, traditionally applied to non-centrosymmetric interfaces such as that between polystyrene and water[66,67], for label-free measurements of the surface potential of individual condensates. SHG is a nonlinear optical phenomenon[68], in which two photons, each with frequency ω, interact with a non-centrosymmetric medium to create a single photon with twice the frequency, 2ω (Fig. 4b). The broken symmetry at the interface causes molecules to have a specific orientation, thereby generating a second-order polarization upon exposure to incident light[69].

We hypothesized that the interfacial electric field of the condensates is strong enough to align molecules at their surfaces, leading to a second-order polarization[70]. Furthermore, this interfacial electric field can induce polarization of water molecules within the surrounding solvent, breaking the centrosymmetry of the water molecules at the interface (Fig. 4b). This leads to the generation of an SHG signal dependent on the surface potential of each condensate[67]. To evaluate whether SHG signals could be detected in our condensates, we applied a pulsed laser excitation at 1,045 nm while detecting the emission with a non-descanned detector centred at 523 nm from condensates incubated for 2 h. Pleasingly, we were able to visualize intense SHG signals directly from the condensates (Fig. 4c). This observation confirms that SHG can be leveraged as a label-free method for visualizing condensates and potentially characterizing their surface potentials.

We next sought to ask whether the SHG signal is correlated with the interfacial potential at the single condensate level. To this end, we first established a theoretical relationship between the second harmonic field, E_{SHG}, the intensity of the SHG signal at the interface, I_{SHG}, and the surface potential of the condensate, φ_0. By assuming the condensate surface to be a planar surface (due to its large diameter of >250 nm), we combined Gouy–Chapman theory[62], which is used to describe the potential profile defined by the surface charge density of a surface and the bulk ionic contents[67,71], with theories for SHG to quantify the surface potential of the condensates (Supplementary Texts 2 and 3)[66,67,71–73]. Experimentally, we dialysed the condensate solution into different salt concentrations. We optimized the two-photon power to ensure that the SHG signal could be detected at all salt and age conditions, allowing for direct comparison of the SHG signal output. We quantified the SHG signals generated by condensates with similar size at different salt conditions and derived the surface potential of condensates aged for 2 h and 24 h using the developed theoretical relationship (Supplementary Texts 2 and 3 and Supplementary Fig. 5a). A significant difference in the surface potential of the condensates was observed between those aged for 2 h and 24 h (Fig. 4d), suggesting a significant difference in the surface charge density of condensates of different ages. We note that, in the fitting function of the SHG signal and surface potential, $I_{SHG} \propto |A + B\Phi_0|^2$, parameters A and B are a function of interfacial water density, molecular orientation and

polarizability[68], which are not the same in condensates of different ages, so the derived surface potential was only used for qualitative comparison. The observed absolute difference in SHG signal in young and old condensates under different conditions in turn reflects the cumulative effect of the changes in surface potential caused by condensate aging. This observation further implies that the aging process can alter the IDP network at the interfacial region of condensates, thereby defining different charge conditions at the condensate surface. As the zeta-potential represents the electric potential outside the shear plane mediated by the surface charge, it can be used to verify our SHG analysis of surface potential. We thus measured the zeta-potential of condensates aged differently and observed a substantially decreased zeta-potential in aged condensates (Supplementary Fig. 5b). This measurement supports that the high surface charge density of young condensates, as evaluated by the SHG effect, enables a stronger attraction of ions onto the condensate, thereby maintaining a larger zeta-potential, which confirms that aging can alter the electric potential profiles of condensates. This finding further suggests that the change in internal structure of condensates with aging also alters the surface structure of the condensates, modulating the surface potential and thus the interfacial potential gradients[74].

Aging-dependent electrochemical activities of condensates

Having unravelled the aging-dependent electrochemical properties of condensates, we next delved into whether these dynamics could influence the emergent physicochemical functions of condensates in their young (2 h) and old (24 h) states. Our hypothesis rested on the notion that the altered overall electrochemical equilibrium of condensates will lead to variations in electric potential-dependent physicochemical functions, such as redox reactions dependent on the interfacial electric field[10] and molecular transport influenced by the electric potential gradient (Fig. 5a).

A previous study demonstrated that the interfacial electric field of condensates can modulate redox reactions through the electric field-mediated oxidation of hydroxyl ions[10]. We thus set out to explore whether the capability of condensates to modulate redox reactions is affected by condensate aging. Utilizing the fluorogenic resazurin assay[10], where the reduction of resazurin to resorufin triggers fluorescence activation, we analysed the reduction capability of condensates of different ages (2 h versus 24 h). Our findings indicated that, in comparison to young condensates, old condensates exhibited a significant decrease in the resorufin fluorescence signal (Fig. 5b), indicating a diminished reduction capability. This behaviour corresponds to decreased interphase electric potential and surface potential in aged condensates.

To uncover the origin of condensate reduction reactions, we scrutinized the ability of condensates to drive oxidation reactions by directly assessing the production of hydroxyl radicals[75] in the supernatant of condensate samples. The ability of condensates to generate free hydroxyl radicals was confirmed by linear ion MS and electron paramagnetic resonance (EPR) (Supplementary Fig. 6). We analysed the quantity of hydrated hydroxyl radicals (H_3O^+–$OH^•$) in young and aged condensates (2 h versus 24 h) using linear ion MS. As hydrated hydroxyl radicals[75,76] have limited stability, the detection of hydroxyl radicals represents the transient electrochemical activity of condensates. We observed a noticeable peak at m/z 36 for young condensates, corresponding to hydrated hydroxyl radicals (Fig. 5c). In contrast, for old condensates, we were unable to detect any signal at m/z 36, indicating a significant weakening of the oxidation capability with condensate aging. This finding is consistent with the aging-dependent capability of condensates to drive reduction reactions and supports the idea that the redox capability of condensates is determined by the age-dependent electrochemical dynamics of condensates.

An electric potential gradient between phases sets up an interfacial potential gradient[55,77]. This potential gradient may act as a trap or barrier, exerting passive physical effects on molecules diffusing across the boundary (Fig. 5d). To assess this possibility, we initially introduced charged fluorescent small molecules into a solution containing condensates of different ages. We examined the spatial distribution of MitoTracker Red FM (Fig. 5e), a positively charged fluorescent molecule[78], with condensates of similar size but varying ages, thereby excluding the potential interfacial effects stemming from size dependence. We found that, in comparison to old condensates (24 h), young condensates exhibited a significantly higher partition coefficient of the small molecule on the interface over the dense phase (Fig. 5f). This observation suggests that the difference between the surface potential and the phase electric potential forms a trap to the free diffusion of molecules.

Inspired by recent studies showing that the interface of condensates can promote fibril formation[47,49], we examined whether the distinct interfacial electrochemical properties of young and old condensates determine their corresponding capability to modulate fibril formation through the field-mediated alignment effect[79]. We doped amyloid-β (1–40) into solutions containing young or old condensates and evaluated the formation of amyloid fibrils in these solutions by employing a typical ThT-based assay for an additional 8 h of incubation (Fig. 5g). The increase in ThT signal correlates with increased β-rich fibril structures[49]. In the solutions containing only condensates, we did not observe noticeable fibril formation or substantially increased ThT signal (Fig. 5h). In the solution containing amyloid and condensates, we found that the interface of young condensates showed a higher ThT signal comparing to the dense phase of condensates (Fig. 5h). This observation supports a previous publication showing that the interface can serve as a scaffold to promote fibril formation[49]. By comparing the ThT distribution of samples with old or young condensates, old condensates showed interconnected star-shaped aggregates extending into the dilute phase of the condensates, whereas young condensates only showed fibril growth primarily at the interfacial region (Fig. 5h). Interestingly, we found that comparing the ThT signal in samples with or without condensates, the existence of condensates suppressed the formation of large amyloid fibrils compared to the solution containing only amyloid (Fig. 5i and Supplementary Fig. 7). These observations suggest that although an interface can have preferential extended molecular structures and a high molecular density to mediate fibril formation[48,49], the interfacial potential gradient of condensates can serve an orthogonal role in confining amyloid protein molecules to the interface, thereby limiting their further growth into an interconnected network, as found in old condensates.

Discussion

The electrochemical environment of a living cell modulates diverse aspects of cellular physiology[9,26,28,80]. However, limited progress has been made in understanding how intracellular electrochemistry is modulated, with most insights derived from studies on ion channels and pumps[81], a set of cross-membrane protein assemblies. Recent discoveries regarding the role of macromolecular condensation in regulating the potentials of water and ions[9,10,18,23,25] shed light on a possible role of condensation in modulating intracellular electrochemistry, but the detailed mechanism by which condensates define and regulate their own electrochemical environments is unknown. Our study demonstrates the detailed mechanism by which the non-equilibrium aging process of biomolecular condensates can tune their electrochemical environments, modulating their pH gradients and interphase and surface electric potentials. The demonstrated correlation between these electrochemical features and the physicochemical functions of condensates strongly suggests the importance of the electrochemical dynamics of condensates for their biological and chemical functions.

The present study emphasizes that the dynamic character of condensates defines their evolving electrochemical properties. The non-equilibrium nature of condensates in solution, driven by processes such as Ostwald ripening and emulsification[36,82], plays a pivotal role

https://doi.org/10.1038/s41557-025-01762-7

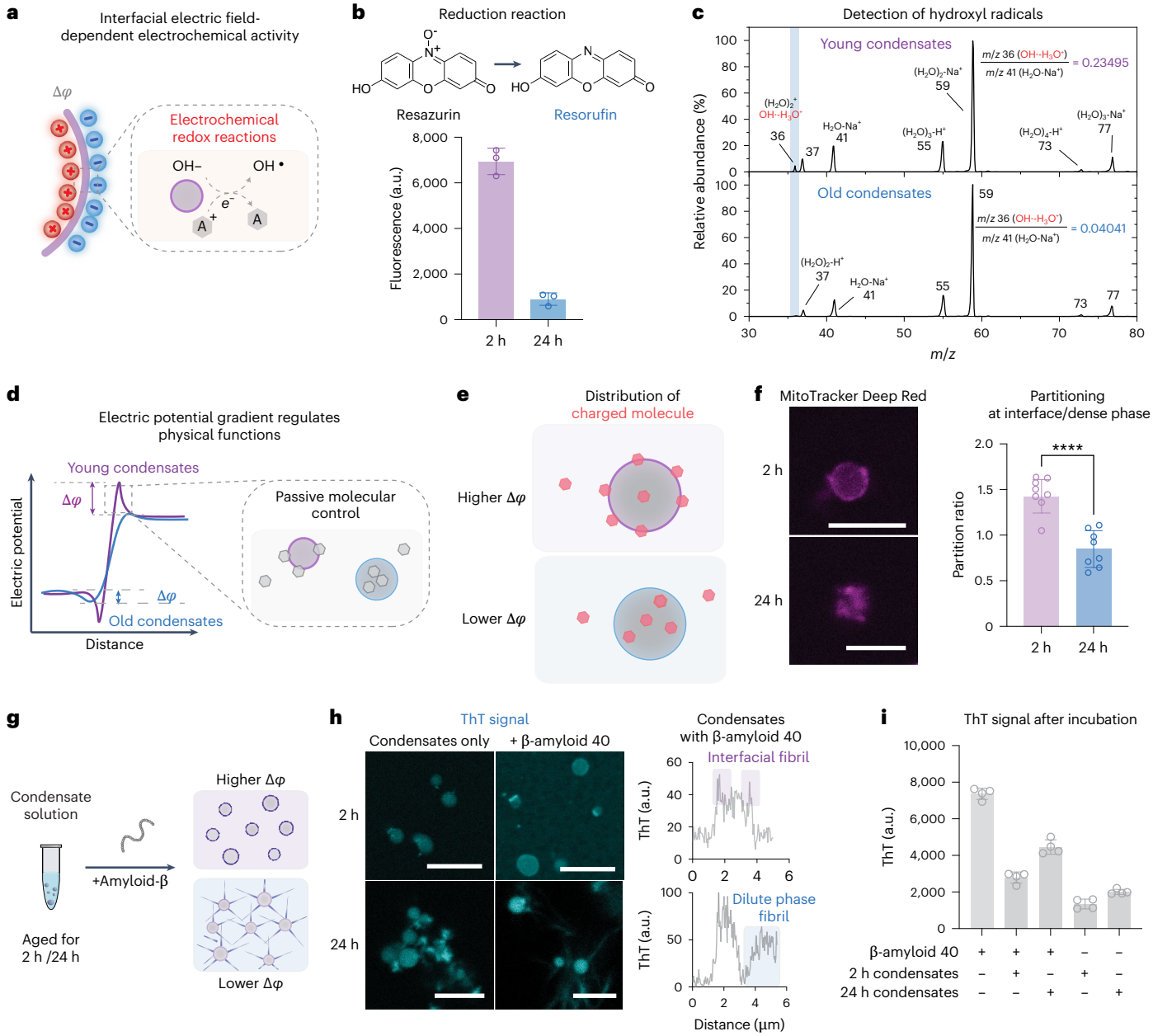

Fig. 5 | The interfacial potential of condensates modulates the electrochemical and physical functions of condensates. a, The interfacial electric field of condensates can drive redox reactions through the generation of free hydroxyl radicals and solvated electrons. **b**, Evaluation of the reduction capability of condensates incubated for 2 h and 24 h using a resazurin assay. Data points represent mean ± s.d. $n = 3$ independent samples. **c**, MS evaluation of the supernatants of condensates incubated for 2 h and 24 h. Only young condensates (incubated for 2 h) showed an m/z peak at 36, which indicates the existence of hydrated hydroxyl radicals. **d**, An electric potential gradient is established between the bulk phase and the interface. This potential gradient forms a trap or barrier, which can passively modulate diffusion of charged molecules. **e**, Evaluation of condensates with distinct interfacial potentials on modulating the partitioning of charged small molecules. **f**, Comparison of the partition coefficient of MitoTracker Deep Red, a positively charged dye, at the interface over the dense phase for condensates incubated for 2 h and 24 h. Scale bars, 5 μm. Statistical analysis was performed using a two-tailed t-test: ****$P < 0.0001$. Data points represent mean ± s.d. $n = 3$ independent samples. **g**, Evaluation of condensates with distinct interfacial potentials on regulating fibril formation of β-amyloid 40. The condensate solution was first incubated for distinct periods before adding the amyloid-β proteins. Amyloid fibril formation was evaluated after 8 h addition of amyloid-β. **h**, Representative images of the ThT signal for condensates (pre-incubated for 2 h and 24 h) with or without the addition of amyloid-β after 8 h of incubation. ThT line profiles are shown for condensate solutions aged differently with added β-amyloid 40. The addition of amyloid-β to young condensates generates a distinct signal at the interfacial regions, and old condensates show an extended ThT signal at the dilute phase. Scale bars, 10 μm. **i**, Comparison of the ThT signal between samples prepared with distinct components. Data points represent mean ± s.d. n = 4 independent samples.

in regulating their forms. The evolving dense-phase interactions constantly alter the interior ionic environments of condensates at different ages. A crucial feature uncovered in this study is that the interfacial region, in which the density gradient of biomolecules is established and the proteins typically adopt expanded conformations[48], undergoes a significant change in ionic content during aging. This feature might serve as the driving force modulating both the dense-phase ion contents and the surface charge density of the condensates. In essence, the present study suggests that the dynamic and evolving nature of condensates in solution contributes to the heterogeneity in their

electrochemical properties and functions. This insight challenges a simplistic view that condensates with the same biomolecular composition will possess identical properties, highlighting the importance of considering the broader context of their formation and aging processes for function characterizations.

The capability of condensates to actively tune their pH and potential gradients suggests a possible way in which condensates can change their electrochemical dynamics to generate proton motive forces[65,83], akin to the properties observed in the cellular membranes that power respiration. From the aspect of function, this proton motive force is also the fundamental driver for redox reactions in mitochondrial membranes[65]. This highlights the similarities in the biophysical properties of the membrane of a cell and the interface of a condensate. However, whether this is an active powering of a proton circuit in the case of condensates remains unclear. It is akin to a hydroelectric dam, where external forces or reactions are needed to actively modulate gradients and drive the flow. We propose that such modulation effects may relate to chemical reactions that can influence the electrochemical potential equilibrium between the dilute and dense phases[10,22,25], thereby generating a driving force to power proton movement.

A unique property of liquid-in-liquid emulsions such as condensates is the surface charge-dependent electric double layer. This layer can provide a repulsion force to protect condensates against coagulation by van der Waals attraction forces, allowing distinct condensates to maintain their individuality during their cellular lifetimes. This emulsification property is proposed to be important for function homeostasis[82]. The electric double layer acts as an active electric field, which can drive redox reactions and modulate molecular alignment. The electric double layer defines the interfacial potential, but the electric potential difference between phases differs from the interfacial potential. This distinction leads to unique functions. The difference in interfacial and phase potentials creates a potential barrier, passively regulating the transport of charged small molecules. These distinctive physical and chemical activities of condensates, influenced by their electrochemical features, underscore that condensates are not inert entities. Expanding the molecular grammar of condensates to understand how electrochemical properties are encoded is crucial for comprehending the global cellular effects arising from their electrochemical functions[18].

Our study has applied an electrochemical potentiometry-based method and an optical method to measure the electric potential difference between phases and the electric potential at the surface. These newly established methods allow us to quantify key electrochemical properties of aqueous two-phase systems. The electrochemical potentiometry-based measurements utilize a well-defined redox reaction to compare the relative change in electric potential at the electrode/dilute phase and electrode/dense phase interfaces, generating an electric potential difference between phases. The SHG-based method further enables us to directly visualize condensates, without the need for external labels, based on their unique interfacial effects[68,70], which arise from the interaction between the interfacial field and the dipoles of water molecules in the diffuse layer, generating a net interfacial dipole capable of sum-frequency generation[84]. Although the interfacial potential is a potential difference at the boundary of each phase, the absolute difference might be difficult to quantity[85,86]. First, the interface is beyond the Stern layer, where the second layer of attractive ions from the bulk solution reside. This is defined by the Gibbs dividing plane[87], which is not optically definable. Second, the thermodynamic potentials of single ionic species are impossible to measure. At a finite distance, such as the interface, the transport of an ion involves chemical and electric work due to the finite size of ions, meaning that the Gibbs energy of the interaction with the surroundings must be non-zero[88]. The contribution of electric and chemical work is ambiguously separable. Therefore, measuring the absolute electric potential difference across a liquid–liquid interface might not be possible. Although mesoscopic measurements of zeta-potential or the electrokinetic potential of condensates can be achieved with an electrophoretic assay[89,90], the applied external electric field might lead to the displacement of surface ions or the displacement of potentials. Thus, deriving the zeta-potential using the Helmholtz–Smoluchovski equation requires further conversion between the displaced charge and potential[91], which is also hard to evaluate. These convoluting aspects of measurements highlight the need for technology to enable interference-free measurements, and emphasize the requirement for an accurate depiction of the condensate structure from the surface to the interface to map the electrochemical features of the condensate, such as establishing the mechanisms by which the surface charge of condensates is defined by the surface residues of condensates.

From a theoretical standpoint, classical mean-field theories rely on defining an average charge density of a surface that is homogeneous and sharp, and these theories are incapable of capturing the interaction between water and localized charge or ion–ion interactions. These factors make classical theories non-ideal for implementation in studies of condensate electrochemistry, because the interfacial region has density and structure fluctuations that define heterogeneity in the charge distributions and physical structure of the condensate surface[47–49,92]. Furthermore, recent works have shown that water molecules within the condensates present a hydrogen-bonded network and different water activities compared to the dilute phase[22,93]. Our demonstration of the generation of SHG signals from condensates also suggests that the centrosymmetric nature of bulk water molecules is broken at the condensate surface. This experimental evidence emphasizes the importance of developing theories to understand the contribution of water to the electrochemical features of condensates, such as how ion–water affinity is altered due to the unique water environment within condensates, as these can promote our understanding of the charging process (for example, overcharging) of condensate surfaces.

In summary, the elucidation of the intricate and evolving electrochemical features of condensates in this study marks a stride forward in understanding the physical chemistry of condensates. Our findings not only provide valuable insights into the nuanced dynamics of condensate aging and behaviour, but also introduce a new dimension to the field of intracellular electrochemistry. The uncovered electrochemical characteristics open up avenues for novel paradigms to understand the physiological relevance of condensates, offering potential applications in diverse areas such as cellular signalling, biomolecular interactions and disease mechanisms. This research paves the way for further exploration and refinement of our understanding of condensate electrochemistry, fostering a deeper comprehension of their roles in cellular processes.

Online content

Any methods, additional references, Nature Portfolio reporting summaries, source data, extended data, supplementary information, acknowledgements, peer review information; details of author contributions and competing interests; and statements of data and code availability are available at https://doi.org/10.1038/s41557-025-01762-7.

References

1. Roden, C. & Gladfelter, A. S. RNA contributions to the form and function of biomolecular condensates. *Nat. Rev. Mol. Cell Biol.* **22**, 183–195 (2021).
2. Banani, S. F., Lee, H. O., Hyman, A. A. & Rosen, M. K. Biomolecular condensates: organizers of cellular biochemistry. *Nat. Rev. Mol. Cell Biol.* **18**, 285–298 (2017).
3. Alberti, S. & Hyman, A. A. Biomolecular condensates at the nexus of cellular stress, protein aggregation disease and ageing. *Nat. Rev. Mol. Cell Biol.* **22**, 196–213 (2021).
4. Dai, Y., You, L. & Chilkoti, A. Engineering synthetic biomolecular condensates. *Nat. Rev. Bioeng.* **1**, 466–480 (2023).

5. Choi, J.-M., Holehouse, A. S. & Pappu, R. V. Physical principles underlying the complex biology of intracellular phase transitions. *Annu. Rev. Biophys.* **49**, 107–133 (2020).
6. Pappu, R. V., Cohen, S. R., Dar, F., Farag, M. & Kar, M. Phase transitions of associative biomacromolecules. *Chem. Rev.* **123**, 8945–8987 (2023).
7. Romero-Perez, P. S., Dorone, Y., Flores, E., Sukenik, S. & Boeynaems, S. When phased without water: biophysics of cellular desiccation, from biomolecules to condensates. *Chem. Rev.* **123**, 9010–9035 (2023).
8. Posey, A. E. et al. Biomolecular condensates are characterized by interphase electric potentials. *J. Am. Chem. Soc.* 10.1021/jacs.4c08946 (2024).
9. Dai, Y. et al. Biomolecular condensates regulate cellular electrochemical equilibria. *Cell* **187**, 5951–5966.e5918 (2024).
10. Dai, Y. et al. Interface of biomolecular condensates modulates redox reactions. *Chem* **9**, 1594–1609 (2023).
11. Kilgore, H. R. & Young, R. A. Learning the chemical grammar of biomolecular condensates. *Nat. Chem. Biol.* **18**, 1298–1306 (2022).
12. Kilgore, H. R. et al. Distinct chemical environments in biomolecular condensates. *Nat. Chem. Biol.* **20**, 291–301 (2024).
13. Ye, S. et al. Micropolarity governs the structural organization of biomolecular condensates. *Nat. Chem. Biol.* **20**, 443–451 (2024).
14. Cakmak, F. P., Choi, S., Meyer, M. O., Bevilacqua, P. C. & Keating, C. D. Prebiotically-relevant low polyion multivalency can improve functionality of membraneless compartments. *Nat. Commun.* **11**, 5949 (2020).
15. Choi, S., Knoerdel, A. R., Sing, C. E. & Keating, C. D. Effect of polypeptide complex coacervate microenvironment on protonation of a guest molecule. *J. Phys. Chem. B* **127**, 5978–5991 (2023).
16. Ausserwöger, H. et al. Quantifying collective interactions in biomolecular phase separation. Preprint at https://doi.org/10.1101/2023.05.31.543137 (2023).
17. King, M. R. et al. Macromolecular condensation organizes nucleolar sub-phases to set up a pH gradient. *Cell* **187**, 1889–1906.e1824 (2024).
18. Watson, J. L. et al. Macromolecular condensation buffers intracellular water potential. *Nature* **623**, 842–852 (2023).
19. Iglesias-Artola, J. M. et al. Charge-density reduction promotes ribozyme activity in RNA–peptide coacervates via RNA fluidization and magnesium partitioning. *Nat. Chem.* **14**, 407–416 (2022).
20. Choi, S., Meyer, M. O., Bevilacqua, P. C. & Keating, C. D. Phase-specific RNA accumulation and duplex thermodynamics in multiphase coacervate models for membraneless organelles. *Nat. Chem.* **14**, 1110–1117 (2022).
21. Cao, S. et al. Dipeptide coacervates as artificial membraneless organelles for bioorthogonal catalysis. *Nat. Commun.* **15**, 39 (2024).
22. Guo, X. et al. Biomolecular condensates can function as inherent catalysts. Preprint at https://doi.org/10.1101/2024.07.06.602359 (2024).
23. Hoffmann, C. et al. Electric potential at the interface of membraneless organelles gauged by graphene. *Nano Lett.* **23**, 10796–10801 (2023).
24. Yan, X. et al. Intra-condensate demixing of TDP-43 inside stress granules generates pathological aggregates. Preprint at https://doi.org/10.1101/2024.01.23.576837 (2024).
25. Dai, Y., Wang, Z.-G. & Zare, R. N. Unlocking the electrochemical functions of biomolecular condensates. *Nat. Chem. Biol.* **20**, 1420–1433 (2024).
26. Lee, D.-yD. et al. Magnesium flux modulates ribosomes to increase bacterial survival. *Cell* **177**, 352–360.e313 (2019).
27. Prindle, A. et al. Ion channels enable electrical communication in bacterial communities. *Nature* **527**, 59–63 (2015).
28. Kikuchi, K. et al. Electrochemical potential enables dormant spores to integrate environmental signals. *Science* **378**, 43–49 (2022).
29. Shin, Y. & Brangwynne, C. P. Liquid phase condensation in cell physiology and disease. *Science* **357**, eaaf4382 (2017).
30. Wolozin, B. & Ivanov, P. Stress granules and neurodegeneration. *Nat. Rev. Neurosci.* **20**, 649–666 (2019).
31. Tsang, B., Pritišanac, I., Scherer, S. W., Moses, A. M. & Forman-Kay, J. D. Phase separation as a missing mechanism for interpretation of disease mutations. *Cell* **183**, 1742–1756 (2020).
32. Brangwynne, C. P., Tompa, P. & Pappu, R. V. Polymer physics of intracellular phase transitions. *Nat. Phys.* **11**, 899–904 (2015).
33. Erkamp, N. A. et al. Spatially non-uniform condensates emerge from dynamically arrested phase separation. *Nat. Commun.* **14**, 684 (2023).
34. Galvanetto, N. et al. Extreme dynamics in a biomolecular condensate. *Nature* **619**, 876–883 (2023).
35. Fritsch, A. W. et al. Local thermodynamics govern formation and dissolution of *Caenorhabditis elegans* P granule condensates. *Proc. Natl Acad. Sci. USA* **118**, e2102772118 (2021).
36. Kirschbaum, J. & Zwicker, D. Controlling biomolecular condensates via chemical reactions. *J. R. Soc. Interface* **18**, 20210255 (2021).
37. Takaki, R., Jawerth, L., Popović, M. & Jülicher, F. Theory of rheology and aging of protein condensates. *PRX Life* **1**, 013006 (2023).
38. Alshareedah, I. et al. Sequence-specific interactions determine viscoelasticity and ageing dynamics of protein condensates. *Nat. Phys* **20**, 1482–1491 (2024).
39. Alshareedah, I., Moosa, M. M., Pham, M., Potoyan, D. A. & Banerjee, P. R. Programmable viscoelasticity in protein–RNA condensates with disordered sticker-spacer polypeptides. *Nat. Commun.* **12**, 6620 (2021).
40. Holehouse, A. S. & Kragelund, B. B. The molecular basis for cellular function of intrinsically disordered protein regions. *Nat. Rev. Mol. Cell Biol.* **25**, 187–211 (2024).
41. Nott, T. J. et al. Phase transition of a disordered nuage protein generates environmentally responsive membraneless organelles. *Mol. Cell* **57**, 936–947 (2015).
42. Dai, Y. et al. Programmable synthetic biomolecular condensates for cellular control. *Nat. Chem. Biol.* **19**, 518–528 (2023).
43. Dzuricky, M., Rogers, B. A., Shahid, A., Cremer, P. S. & Chilkoti, A. De novo engineering of intracellular condensates using artificial disordered proteins. *Nat. Chem.* **12**, 814–825 (2020).
44. Tan, C., Saurabh, S., Bruchez, M. P., Schwartz, R. & LeDuc, P. Molecular crowding shapes gene expression in synthetic cellular nanosystems. *Nat. Nanotechnol.* **8**, 602–608 (2013).
45. Shen, Y. et al. The liquid-to-solid transition of FUS is promoted by the condensate surface. *Proc. Natl Acad. Sci. USA* **120**, e2301366120 (2023).
46. Emmanouilidis, L. et al. NMR and EPR reveal a compaction of the RNA-binding protein FUS upon droplet formation. *Nat. Chem. Biol.* **17**, 608–614 (2021).
47. Emmanouilidis, L. et al. A solid beta-sheet structure is formed at the surface of FUS droplets during aging. *Nat. Chem. Biol.* **20**, 1044–1052 (2024).
48. Farag, M. et al. Condensates formed by prion-like low-complexity domains have small-world network structures and interfaces defined by expanded conformations. *Nat. Commun.* **13**, 7722 (2022).
49. Linsenmeier, M. et al. The interface of condensates of the hnRNPA1 low-complexity domain promotes formation of amyloid fibrils. *Nat. Chem.* **15**, 1340–1349 (2023).
50. Mangiarotti, A., Chen, N., Zhao, Z., Lipowsky, R. & Dimova, R. Wetting and complex remodeling of membranes by biomolecular condensates. *Nat. Commun.* **14**, 2809 (2023).

51. Chen, B. et al. Water–solid contact electrification causes hydrogen peroxide production from hydroxyl radical recombination in sprayed microdroplets. *Proc. Natl Acad. Sci. USA* **119**, e2209056119 (2022).
52. Lin, S., Cao, L. N. Y., Tang, Z. & Wang, Z. L. Size-dependent charge transfer between water microdroplets. *Proc. Natl Acad. Sci. USA* **120**, e2307977120 (2023).
53. Trefalt, G., Behrens, S. H. & Borkovec, M. Charge regulation in the electrical double layer: ion adsorption and surface interactions. *Langmuir* **32**, 380–400 (2016).
54. Vis, M. et al. Effects of electric charge on the interfacial tension between coexisting aqueous mixtures of polyelectrolyte and neutral polymer. *Macromolecules* **48**, 7335–7345 (2015).
55. Zhang, P. & Wang, Z.-G. Interfacial structure and tension of polyelectrolyte complex coacervates. *Macromolecules* **54**, 10994–11007 (2021).
56. Chen, G. Donnan equilibrium revisited: coupling between ion concentrations, osmotic pressure and Donnan potential. *J. Micromech. Mol. Phys.* **7**, 127–134 (2022).
57. Vis, M., Peters, V. F., Tromp, R. H. & Erné, B. H. Donnan potentials in aqueous phase-separated polymer mixtures. *Langmuir* **30**, 5755–5762 (2014).
58. Stepanov, V. P. & Kulik, N. P. Galvani potential at liquid-liquid interfaces for dissolving AgBr+LiCl and AgI+LiCl melts. *Ionics* **24**, 2851–2856 (2018).
59. Li, L. et al. Phase behavior and salt partitioning in polyelectrolyte complex coacervates. *Macromolecules* **51**, 2988–2995 (2018).
60. Iqbal, M. et al. Aqueous two-phase system (ATPS): an overview and advances in its applications. *Biol. Proc. Online* **18**, 18 (2016).
61. Haynes, C. A., Carson, J., Blanch, H. W. & Prausnitz, J. M. Electrostatic potentials and protein partitioning in aqueous two-phase systems. *AIChE J.* **37**, 1401–1409 (1991).
62. Bard, A. J., Faulkner, L. R. & White, H. S. *Electrochemical Methods: Fundamentals and Applications* (Wiley, 2022).
63. Lamoureux, G. & Roux, B. Absolute hydration free energy scale for alkali and halide ions established from simulations with a polarizable force field. *J. Phys. Chem. B* **110**, 3308–3322 (2006).
64. Criss, C. M. & Luksha, E. Thermodynamic properties of nonaqueous solutions. IV. Free energies and entropies of solvation of some alkali metal halides in *N*,*N*-dimethylformamide. *J. Phys. Chem.* **72**, 2966–2970 (1968).
65. Dzbek, J. & Korzeniewski, B. Control over the contribution of the mitochondrial membrane potential (ΔΨ) and proton gradient (ΔpH) to the protonmotive force (Δp): in silico studies. *J. Biol. Chem.* **283**, 33232–33239 (2008).
66. Eisenthal, K. B. Second harmonic spectroscopy of aqueous nano- and microparticle interfaces. *Chem. Rev.* **106**, 1462–1477 (2006).
67. Yan, E. C. Y., Liu, Y. & Eisenthal, K. B. New method for determination of surface potential of microscopic particles by second harmonic generation. *J. Phys. Chem. B* **102**, 6331–6336 (1998).
68. Corn, R. M. & Higgins, D. A. Optical second harmonic generation as a probe of surface chemistry. *Chem. Rev.* **94**, 107–125 (1994).
69. Didier, M. E. P., Tarun, O. B., Jourdain, P., Magistretti, P. & Roke, S. Membrane water for probing neuronal membrane potentials and ionic fluxes at the single cell level. *Nat. Commun.* **9**, 5287 (2018).
70. Jin, L. et al. Characterization and application of a new optical probe for membrane lipid domains. *Biophys. J.* **90**, 2563–2575 (2006).
71. Liu, Y., Yan, E. C. Y., Zhao, X. & Eisenthal, K. B. Surface potential of charged liposomes determined by second harmonic generation. *Langmuir* **17**, 2063–2066 (2001).
72. Zhao, X., Ong, S. & Eisenthal, K. B. Polarization of water molecules at a charged interface. Second harmonic studies of charged monolayers at the air/water interface. *Chem. Phys. Lett.* **202**, 513–520 (1993).
73. Ong, S., Zhao, X. & Eisenthal, K. B. Polarization of water molecules at a charged interface: second harmonic studies of the silica/water interface. *Chem. Phys. Lett.* **191**, 327–335 (1992).
74. Israelachvili, J. N. *Intermolecular and Surface Forces* (Academic Press, 2011).
75. Xing, D. et al. Capture of hydroxyl radicals by hydronium cations in water microdroplets. *Angew. Chem. Int. Ed.* **61**, e202207587 (2022).
76. Finkelstein, E., Rosen, G. M. & Rauckman, E. J. Spin trapping of superoxide and hydroxyl radical: practical aspects. *Arch. Biochem. Biophys.* **200**, 1–16 (1980).
77. Majee, A., Weber, C. A. & Jülicher, F. Charge separation at liquid interfaces. *Phys. Rev. Res.* **6**, 033138 (2024).
78. Lhee, S. et al. Spatial localization of charged molecules by salt ions in oil-confined water microdroplets. *Sci. Adv.* **6**, eaba0181 (2020).
79. Campioni, S. et al. The presence of an air-water interface affects formation and elongation of α-synuclein fibrils. *J. Am. Chem. Soc.* **136**, 2866–2875 (2014).
80. Humphries, J. et al. Species-independent attraction to biofilms through electrical signaling. *Cell* **168**, 200–209.e212 (2017).
81. Jentsch, T. J., Hübner, C. A. & Fuhrmann, J. C. Ion channels: function unravelled by dysfunction. *Nat. Cell Biol.* **6**, 1039–1047 (2004).
82. Söding, J., Zwicker, D., Sohrabi-Jahromi, S., Boehning, M. & Kirschbaum, J. Mechanisms for active regulation of biomolecular condensates. *Trends Cell Biol.* **30**, 4–14 (2020).
83. Simon, J., van Spanning, R. J. M. & Richardson, D. J. The organisation of proton motive and non-proton motive redox loops in prokaryotic respiratory systems. *Biochim. Biophys. Acta* **1777**, 1480–1490 (2008).
84. Yan, E. C., Fu, L., Wang, Z. & Liu, W. Biological macromolecules at interfaces probed by chiral vibrational sum frequency generation spectroscopy. *Chem. Rev.* **114**, 8471–8498 (2014).
85. Lyklema, J. Interfacial potentials: measuring the immeasurable? *Substantia* **1**, 75–93 (2017).
86. Gonella, G. et al. Water at charged interfaces. *Nat. Rev. Chem.* **5**, 466–485 (2021).
87. Guggenheim, E. The thermodynamics of interfaces in systems of several components. *Trans. Faraday Soc.* **35**, 397–412 (1940).
88. Zukoski, C. IV & Saville, D. The interpretation of electrokinetic measurements using a dynamic model of the stern layer: I. The dynamic model. *J. Colloid Interface Sci.* **114**, 32–44 (1986).
89. Welsh, T. J. et al. Surface electrostatics govern the emulsion stability of biomolecular condensates. *Nano Lett.* **22**, 612–621 (2022).
90. Kwok, K. Y., Mckenzie, D. L., Evers, D. L. & Rice, K. G. Formulation of highly soluble poly (ethylene glycol)-peptide DNA condensates. *J. Pharm. Sci.* **88**, 996–1003 (1999).
91. Lyklema, J. & Overbeek, J. T. G. On the interpretation of electrokinetic potentials. *J. Colloid Sci.* **16**, 501–512 (1961).
92. Morelli, C. et al. RNA modulates hnRNPA1A amyloid formation mediated by biomolecular condensates. *Nat. Chem.* **16**, 1052–1061 (2024).
93. Joshi, A. et al. Hydrogen-bonded network of water in phase-separated biomolecular condensates. *J. Phys. Chem. Lett.* **15**, 7724–7734 (2024).

Methods

Protein expression and purification

Expression. BL21 (DE3) competent *Escherichia coli* was transformed with the RLP_{WT} gene and plated for kanamycin selection. A single colony was picked and grown overnight in 5 ml of 2×YT liquid medium with 45 μg ml^{-1} kanamycin at 37 °C in a shaking incubator. The culture was then inoculated into 1 l of 2×YT liquid medium with 45 μg ml^{-1} kanamycin and grown at 37 °C with shaking. Protein production was induced by adding isopropyl β-D-1-thiogalactopyranoside at a final concentration of 0.5 mM when the optical density at 600 nm reached 0.5.

Purification of RLP (sequence, SKGP-[GRGDSPYS]20-GY). Cells were collected the next day by centrifugation (Eppendorf High-Speed Centrifuge CR22N) at 2,000*g* for 20 min at 4 °C. The cell pellet from each litre of bacterial culture was resuspended in 30 ml of resuspension buffer (50 mM Tris pH 7.5), and the cell suspension was lysed by 3 min of sonication on ice (each cycle with 10 s on, 40 s off, 75% amplitude). The cell lysate was centrifuged at 25,000*g* for 25 min at 4 °C (Eppendorf High-Speed Centrifuge CR22N). The purification was carried out using the principle of the inverse temperature cycle following the upper critical solution transition behaviour[94,95]. After centrifugation, the supernatant was removed and the insoluble pellet resuspended in 10 ml of urea buffer (50 mM Tris, 500 mM NaCl, 8 M urea, pH 7.5) supplied with 1 μl (≥250 units) of benzonase nuclease (Millipore) per litre of bacterial culture. The protein sample was incubated at room temperature for at least 1 h with rocking to allow the RLP protein to dissolve. The sample was then warmed to 40 °C and centrifuged at 25,000*g* for 25 min at 40 °C (Eppendorf High-Speed Centrifuge CR22N). The supernatant was collected and dialysed into resuspension buffer (50 mM Tris, pH 7.5) for 3 h at 4 °C to trigger a phase transition. The buffer was changed once within this period. After dialysis, the solution in the dialysis tube was centrifuged at 25,000*g* for 25 min at 4 °C. The supernatant was discarded, and the insoluble portion containing the RLP protein was dissolved in urea buffer (50 mM Tris, 500 mM NaCl, 8 M urea, pH 7.5) for 1 h at room temperature. The protein sample was then warmed to 40 °C and centrifuged at 25,000*g* for 25 min at 40 °C. After completing a full cycle of temperature cycle for RLP, the protein purity was checked on a Mini-PROTEAN TGX SDS–PAGE gel (Bio-Rad) with Simply Blue SafeStain (Invitrogen) staining. This concluded the first round of inverse temperature cycle. An additional two cycles were conducted (>88%). RLP protein was then applied to an AKTA Pure chromatography system (Cytiva) with a size-exclusion column (Superdex Increase 75) to reach a final purity of >95%. The RLP protein sample was then dialysed into high salt buffer (50 mM Tris, 500 mM NaCl, pH 7.5) for 4 h at room temperature. The buffer was changed at least three times. After dialysis, minor aggregates were discarded by centrifugation at 1,000*g* for 5 min at 37 °C. The concentration of the supernatant was adjusted to 100 μM and aliquoted into 200-μl tubes and flash-frozen by liquid nitrogen and stored at −80 °C. This solution was the protein stock solution.

Condensate sample preparation

For confocal microscopy characterization of pH. Purified RLP protein stock solution (stored in 50 mM Tris, 500 mM NaCl, pH 7.5) was added to a dilution buffer containing 50 mM Tris and 10% polyethylene glycol 8000 (PEG-8000, Sigma Aldrich) solution (pH 7.5) at a ratio of 3:7, followed by incubation at room temperature for different periods of time. PEG-8000 is not necessary for the formation of condensates. The same dilution process from the stock solution to the dilution buffer containing 50 mM Tris (pH 7.5) was able to mediate condensate formation, but quantification of the condensates under confocal microscopy was constrained at the initial time points due to the small size of the condensates.

For salt-dependent SHG and electrochemical potentiometry. To prepare condensates in distinct salt conditions, we dialysed the stock solution in different salt conditions in buffer containing 50 mM Tris and different salt concentrations/types (pH 7.5). The sample was dialysed for 3 h at room temperature, and the dialysis buffer was changed every 1 h. A change in the turbidity of the samples was typically observed in the third round of dialysis (monitored by the absorbance at 600 nm with the initial internal pH being similar to the sample prepared with the dilution method), after which we extracted the samples and incubated the sample at room temperature for the aging process.

Confocal imaging for the analysis of pH

SNARF-4F 5-(and-6)-carboxylic acid (Thermo Fisher) was added to the condensate solution at a final concentration of 200 nM, 30 min before confocal fluorescence imaging. The sample was placed on a MatTek microwell plate no. 1.5 glass with a 7-mm sample holder (MATTEK). Confocal fluorescence images were taken using a Leica SP8 microscope with a ×40 objective (oil immersion) lens. The excitation wavelength was set at 488 nm with a power intensity of 20%. The emission was detected by two HyD detectors with detecting emission ranges of 540–605 nm (channel 1) and 615–670 nm (channel 2). Both HyD detectors had a gain set fixed at 100%. DIC images were acquired simultaneously under the same excitation set-up with voltage set at ~250 V.

Ratiometric images were generated using the ImageJ Calculator Plus Function to calibrate and quantify pH, which involved dividing the raw imaging signals from channel 2 by those from channel 1 in a co-localized manner. The particle analysis function in ImageJ was used to define the region of interest for individual condensates and further quantification of the size, circularity and mean pixel intensity of individual condensates.

ThT assay tracking of the aging of condensates

ThT was used to track the enhancement of internal intermolecular interactions in the dense phase of condensates upon aging. The ThT was first prepared in dilution buffer, and condensate formation was triggered by means of a dilution assay with a final ThT concentration of 40 μM. A control sample was prepared using the same dilution assay with a final protein concentration of 2 μM, which is below the saturation concentration (C_{sat}) of RLP. Both solutions were transferred to a 384-well plate and sealed with microplate sealing tape (Corning) to prevent evaporation. The ThT signal was tracked using a SPARK multimode microplate reader (Tecan Life Sciences) with excitation at 435 nm (bandwidth of 20 nm), emission at 490 nm (bandwidth of 10 nm) and 10% gain at 25 °C without shaking. The ThT signal of the condensate solution was baseline-corrected with the ThT signal of the control sample using the baseline correction function in GraphPad Prism.

Electrochemical potentiometry

Phase electric potential difference measurements were carried out in a 40-ml high-speed polycarbonate centrifuge tube (Thermo Scientific). Due to the size of the electrode and the volume of the dense phase required for analysis, for reproducible measurements, 15 ml of condensate solution was needed for this analysis. The condensate solutions (2 h and 24 h) were incubated at room temperature and then centrifuged at 4 °C at 25,000*g* for 25 min to separate the phases. As shown schematically in Fig. 3b, two identical Ag/AgCl reference electrodes were used to measure the potential difference between the two phases. Before the electrodes were immersed in solution, the electrodes were rinsed with plenty of deionized water and gently dried with a paper towel. The potential difference between the two electrodes immersed in the dilute phase was used as the baseline following a similar strategy as published previously[96]. Two Ag/AgCl electrodes were respectively immersed into the dense phase and dilute phase. To check that the measured potential was symmetric with respect to the baseline, electrodes were exchanged between the two phases during each measurement. Open-circuit electric potentials were recorded as a function of time at intervals of 0.1 s for 10 s with a Metrohm Autolab

PGSTAT204 station (measurements longer than 10 s are not reproducible due to possible breakage of the phase boundary resulting in the exchange of ions between phases).

SHG imaging of surface potential of individual condensates

We applied the theories in Supplementary Text for SHG imaging of the surface potential of the condensates. We used a Leica SP8 DIVE Multiphoton microscope with an excitation set with a multiphoton laser at 1,045 nm. A HYD non-descanned detector was applied to collect the signal in the range of 515–535 nm. The same z depth was used to evaluate condensates to account for the possible interfacial effect caused by the solid–liquid contact on the imaging glass surface. MATLAB was used to analyse the SHG signal generated from the interface region (defined as the sharp intensity difference between the dilute phase and the first pixel around the condensates). Based on the fitting equation derived in Supplementary Text, we used the same condition to perform SHG imaging of individual condensates for samples incubated for 2 h and 24 h and obtained their surface potential from their SHG signal.

Zeta-potential measurements

Electrophoretic mobility was measured using a Malvern ZEN3600 (Malvern Panalytical BV) device. Zeta-potential of condensates (prepared in 10 mM NaCl condition) was measured with a DTS1070 cell of polycarbonate material at room temperature with Henry's function ($f(\kappa a)=1.5$).

Linear ion trap MS analyses

The condensate samples were prepared as in the phase separation assay. The mixed solution was incubated at room temperature (25 °C). After incubation, the samples were filtered with centrifugal filters (Amicon Ultra-0.5 ml, 30 K) to remove the condensates. The filtered samples were analysed using an LTQ-XL linear ion trap mass spectrometer (Thermo Fisher). The nano-ESI mode was used for sample introduction, and samples were tested in positive ion mode with an applied voltage of 1.2 kV.

Analysis by EPR spectroscopy

5,5-Dimethyl-1-pyrroline-*N*-oxide was used as the hydroxyl radical trapping agent and was added to the supernatant phase of the solution with RLP condensates at one-tenth of the total volume. EPR spectra were recorded at room temperature on a continuous-wave EPR spectrometer (Bruker) with a microwave power of 6.3 mW, a modulation frequency of 100 kHz and a modulation amplitude of up to 5 G.

Resazurin assay

Condensates were first aged for different periods before the addition of 1 mM resazurin stock solution into the condensate solution to a final resazurin concentration of 20 μM. The resazurin assay was incubated for 5 min at room temperature before characterization by a Spark multimode plate reader (Tecan) with an excitation wavelength of 530 nm and emission wavelength of 585 nm.

Charged small molecule assay

Condensates were first aged for different periods before the addition of 2 mM MitoTracker Deep Red FM solution into the condensate solution to a final dye concentration of 500 nM. The sample was directly analysed after adding the dyes. Confocal imaging was conducted with a Leica SP8 system with an excitation laser set to 638 nm and HYD detector set in the range of 650–700 nm.

Amyloid fibril assay

The amyloid monomer stock was prepared as described in a previous study[97,98]. Condensates were first aged for different periods before the addition of amyloid-β1–40 rat (Sigma Aldrich, SCP0037) stock into the condensate solution to a final amyloid concentration at 95 μM, which is above the threshold aggregation concentration. The fibrilization process was analysed by ThT assay (with a final concentration of 20 μM) in a Spark multimode plate reader (Tecan) with an excitation wavelength of 450 nm and emission wavelength of 480 nm at 37 °C for an additional 8 h. For confocal imaging of amyloid fibrils with the Leica SP8 microscope, the excitation laser was set at 405 nm with the HYD detector set in the range 470–500 nm.

Reporting summary

Further information on research design is available in the Nature Portfolio Reporting Summary linked to this article.

Data availability

All relevant data are included with the paper and its related Supplementary Information. Source data are provided with this paper.

References

94. Quiroz, F. G. & Chilkoti, A. Sequence heuristics to encode phase behaviour in intrinsically disordered protein polymers. *Nat. Mater.* **14**, 1164–1171 (2015).
95. Meyer, D. E. & Chilkoti, A. Purification of recombinant proteins by fusion with thermally-responsive polypeptides. *Nat. Biotechnol.* **17**, 1112–1115 (1999).
96. King, R. S., Blanch, H. W. & Prausnitz, J. M. Molecular thermodynamics of aqueous two-phase systems for bioseparations. *AlChE J.* **34**, 1585–1594 (1988).
97. Knowles, T. P. J. et al. Kinetics and thermodynamics of amyloid formation from direct measurements of fluctuations in fibril mass. *Proc. Natl Acad. Sci. USA* **104**, 10016–10021 (2007).
98. Meisl, G. et al. Molecular mechanisms of protein aggregation from global fitting of kinetic models. *Nat. Protoc.* **11**, 252–272 (2016).

Acknowledgements

We acknowledge experimental support from the Center for Biomolecular Condensates and the Biology Imaging Facility of Washington University in St Louis. We appreciate helpful discussions with Z.-G. Wang's group at California Institute of Technology.
We acknowledge funding support from the McKelvy School of Engineering of Washington University in St Louis. Part of this work was supported by the Air Force Office of Scientific Research (FA9550-21-1-0170 to R.N.Z.).

Author contributions

Y.D. generated the idea for this article. Y.D., G.H. and R.N.Z. devised the study. W.Y., X.G., Y.X., Y.M., Z.T., L.Y. and X.S. conducted the experiments. X.G., Y.X., W.Y., Y.M., L.Y. and Z.T. analysed the data. Y.D., G.H. and R.N.Z. wrote the paper, and all authors commented on the paper.

Competing interests

The authors declare no competing interests.

Additional information

Supplementary information The online version contains supplementary material available at https://doi.org/10.1038/s41557-025-01762-7.

Correspondence and requests for materials should be addressed to Richard N. Zare, Guosong Hong or Yifan Dai.

Peer review information *Nature Chemistry* thanks Ellen Adams, Ben Erne, Drgomir Milovanovic, Mario Tagliazucchi and the other, anonymous, reviewer(s) for their contribution to the peer review of this work.

nature portfolio

Corresponding author(s): Yifan Dai

Last updated by author(s): Dec 12, 2024

Reporting Summary

Nature Portfolio wishes to improve the reproducibility of the work that we publish. This form provides structure for consistency and transparency in reporting. For further information on Nature Portfolio policies, see our Editorial Policies and the Editorial Policy Checklist.

Statistics

For all statistical analyses, confirm that the following items are present in the figure legend, table legend, main text, or Methods section.

n/a	Confirmed
☐	☒ The exact sample size (*n*) for each experimental group/condition, given as a discrete number and unit of measurement
☐	☒ A statement on whether measurements were taken from distinct samples or whether the same sample was measured repeatedly
☐	☒ The statistical test(s) used AND whether they are one- or two-sided *Only common tests should be described solely by name; describe more complex techniques in the Methods section.*
☒	☐ A description of all covariates tested
☒	☐ A description of any assumptions or corrections, such as tests of normality and adjustment for multiple comparisons
☒	☐ A full description of the statistical parameters including central tendency (e.g. means) or other basic estimates (e.g. regression coefficient) AND variation (e.g. standard deviation) or associated estimates of uncertainty (e.g. confidence intervals)
☒	☐ For null hypothesis testing, the test statistic (e.g. *F*, *t*, *r*) with confidence intervals, effect sizes, degrees of freedom and *P* value noted *Give P values as exact values whenever suitable.*
☒	☐ For Bayesian analysis, information on the choice of priors and Markov chain Monte Carlo settings
☒	☐ For hierarchical and complex designs, identification of the appropriate level for tests and full reporting of outcomes
☒	☐ Estimates of effect sizes (e.g. Cohen's *d*, Pearson's *r*), indicating how they were calculated

Our web collection on statistics for biologists contains articles on many of the points above.

Software and code

Policy information about availability of computer code

Data collection	NOVA 2.1.6；Las X Life science microscopy software;LTQ Orbitrap software (2.5.5)
Data analysis	GraphPad Prism 10.2.2, Image J (NIH)

For manuscripts utilizing custom algorithms or software that are central to the research but not yet described in published literature, software must be made available to editors and reviewers. We strongly encourage code deposition in a community repository (e.g. GitHub). See the Nature Portfolio guidelines for submitting code & software for further information.

Data

Policy information about availability of data

All manuscripts must include a data availability statement. This statement should provide the following information, where applicable:

- Accession codes, unique identifiers, or web links for publicly available datasets
- A description of any restrictions on data availability
- For clinical datasets or third party data, please ensure that the statement adheres to our policy

All relevant data are included in the manuscript. Source data will be provided with the final version of this manuscript.

Research involving human participants, their data, or biological material

Policy information about studies with human participants or human data. See also policy information about sex, gender (identity/presentation), and sexual orientation and race, ethnicity and racism.

Reporting on sex and gender	N/A
Reporting on race, ethnicity, or other socially relevant groupings	N/A
Population characteristics	N/A
Recruitment	N/A
Ethics oversight	N/A

Note that full information on the approval of the study protocol must also be provided in the manuscript.

Field-specific reporting

Please select the one below that is the best fit for your research. If you are not sure, read the appropriate sections before making your selection.

☒ Life sciences ☐ Behavioural & social sciences ☐ Ecological, evolutionary & environmental sciences

For a reference copy of the document with all sections, see nature.com/documents/nr-reporting-summary-flat.pdf

Life sciences study design

All studies must disclose on these points even when the disclosure is negative.

Sample size	The sample size for each experiments was described under the corresponding figure.
Data exclusions	We performed no data exclusion in this study.
Replication	All experiments were repeated at least three times in this study.
Randomization	N/A
Blinding	N/A

Reporting for specific materials, systems and methods

We require information from authors about some types of materials, experimental systems and methods used in many studies. Here, indicate whether each material, system or method listed is relevant to your study. If you are not sure if a list item applies to your research, read the appropriate section before selecting a response.

Materials & experimental systems

n/a	Involved in the study
☒	☐ Antibodies
☒	☐ Eukaryotic cell lines
☒	☐ Palaeontology and archaeology
☒	☐ Animals and other organisms
☒	☐ Clinical data
☒	☐ Dual use research of concern
☒	☐ Plants

Methods

n/a	Involved in the study
☒	☐ ChIP-seq
☒	☐ Flow cytometry
☒	☐ MRI-based neuroimaging

Plants

Seed stocks	This study did not include any plant as experimental material.
Novel plant genotypes	N/A
Authentication	N/A